PHYSICAL REVIEW A **82**, 042708 (2010)

Absolute energy-resolved measurements of the $H^- + H \rightarrow H_2 + e^-$ associative detachment reaction using a merged-beam apparatus

H. Bruhns,[1,*] H. Kreckel,[1,†] K. A. Miller,[1] X. Urbain,[2] and D. W. Savin[1]

[1]*Columbia Astrophysics Laboratory, Columbia University, 550 West 120th Street, New York, New York 10027-6601, USA*

[2]*Institute of Condensed Matter and Nanosciences, Université Catholique de Louvain, Chemin du Cyclotron 2, B-1348 Louvain-la Neuve, Belgium*

(Received 26 July 2010; published 19 October 2010)

Using a merged-beam configuration, we have performed absolute measurements for the associative detachment reaction $H^- + H \rightarrow H_2 + e^-$. Our energy-resolved measurements for this process remove a long-standing discrepancy between theory and experiment for this fundamental reaction. In particular, we find excellent agreement with theoretical results which previously seemed to be ruled out by earlier experiments performed using a flowing afterglow technique.

DOI: 10.1103/PhysRevA.82.042708 PACS number(s): 34.50.Lf, 52.20.Hv, 95.30.Ft, 97.10.Bt

I. INTRODUCTION

Anion-neutral reactions are important for a wide range of disciplines such as physics, chemistry, astrophysics, ion source technology, plasma processing, and planetary atmospheres. This has been briefly reviewed in [1]. The most fundamental of all anion-neutral reactions is the associative detachment (AD) process

$$H^- + H \rightarrow H_2^- \rightarrow H_2 + e^-. \quad (1)$$

Given the simplicity of this reaction, one would naively expect it to be well understood. Surprisingly, this is not the case. Despite over 40 years of study, experiment and theory have failed to converge in either the magnitude or energy dependence for this reaction.

Early flowing afterglow work quoted a factor of 2 uncertainty [2,3]. A more recent flowing afterglow measurement reports error bars of 30% [4]. All three experiments were performed at 300 K. To within their respective error bars, these measurements show reasonable agreement with the Langevin rate coefficient as well as with the theoretical results of [5], [6], and [7]. But the measurements are all discrepant, at greater than a 1σ level, with the theoretical results of [8] and [9,10].

This comparison would tend to make one question the calculations of [8] and [9,10]. However, the situation is not that simple. The three most recent calculations are those of [7], [8], and [9,10]. All of these calculations used the same potential for the short-lived, intermediate H_2^- complex. So it is surprising that the theoretical results from these three groups have not converged. Additionally, the experimental results of [2], [3], and [4] provide no information on the energy or temperature dependence of the reaction. This limits the ability of these measurements to benchmark theory. In fact the authors in the recent experimental study of [4] write "an accurate temperature variable experimental study would provide a valuable benchmark for theoretical assessments."

Clearly, an energy-resolved measurement of reaction (1) using an independent experimental method is needed. To that end, we have developed a merged-beam apparatus to perform energy-resolved studies for reaction (1). This approach is free of many of the systematic uncertainties to which flowing afterglows may be prone. A detailed description of the apparatus can be found in [1]. The implications of our results for cosmology and first star formation are presented in [10].

Here we describe in detail both the measurement technique and our experimental results. The rest of this paper is organized as follows: In Sec. II we briefly review our experimental approach. Sections III–VII discuss our measurements of the various experimental parameters required to put the results on an absolute scale. The data acquisition procedure is described in Sec. VIII and the error budget is summarized in Sec. IX. Results are presented in Sec. X and a discussion is given in Sec. XI. Section XII summarizes our work.

II. MEASUREMENT TECHNIQUE

A. Apparatus configuration

Beginning with a negatively biased duoplasmatron anion source, we extract a beam of negative particles and select the H^- ions using a Wien filter. The beam energy is $E_{H^-} = -e(U_s + U_f/2)$ where e is the unit charge, $U_s = -10$ kV is the nominal source voltage, and U_f is a small correction voltage defined below. Using a series of standard ion optical elements, this H^- beam is shaped and steered for optimum transmission [1]. A 90° deflection of the beam between the first and second legs of the apparatus prevents ultraviolet photons or neutral atoms and molecules from the source from having a direct path to the interaction region. Beam profiles are observed before and after this deflection using rotating wire beam profile monitors (BPMs), with BPM1 located before the deflector and BPM2 after.

In the second leg (Fig. 1), the beam is brought into the photodetachment chamber which houses a floating cell biased to a potential U_f. Depending on the sign of U_f, the H^- is either accelerated or decelerated upon entering the cell. Once inside, the H^- intersects a 975 nm (1.25 eV) laser beam of 1.4 kW continuous wave (cw) power, at an angle of $\phi = 2.74°$, converting a fraction of the H^- to atomic H. Given the photon energy and number density used, photodetachment can produce only ground state H. Approximately 7.5% of

*Present address: Inficon GmbH, D-50968 Cologne, Germany.
†Present address: Department of Chemistry, University of Illinois, 600 South Mathews Avenue, Urbana, Il 61801, USA.

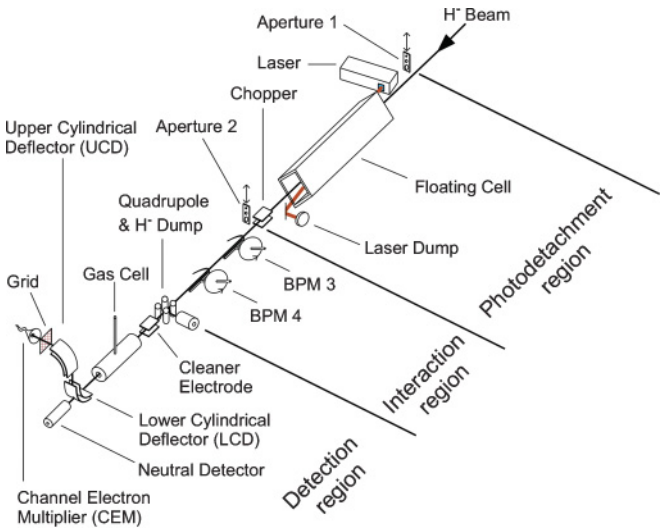

FIG. 1. (Color) Overview for the second leg of the apparatus. Not shown are rectangular magnet coils that are mounted from the beginning of the photodetachment region to the end of the interaction region to compensate for the magnetic field of the Earth.

the H^- beam is converted into an H beam at an energy of $E_H = -e(U_s - U_f/2)$. The resulting merged beams exit the floating cell, whereupon the H^- beam returns to its initial energy while the H beam energy remains unchanged. Beam collimation is provided by two circular 5-mm-diameter apertures separated by ~280 cm, with one located before the photodetachment chamber (aperture 1) and the other after (aperture 2).

The beginning of the beam-beam interaction region is defined by a "chopping" electrode located shortly before aperture 2. By applying a negative voltage to this electrode we can deflect the H^- beam into the vacuum chamber wall and thereby turn off beam-beam reactions in the interaction region. The H beam is chopped by switching the laser on and off. Chopping of both beams out of phase allows us to extract the signal due to H_2 generated in the interaction region from the various backgrounds (e.g., H_2 generated before the interaction region).

Within the interaction region, the relative energy E_r between the beams is given by [11]

$$E_r = \mu\left(\frac{E_{H^-}}{m_{H^-}} + \frac{E_H}{m_H} - 2\sqrt{\frac{E_{H^-}E_H}{m_{H^-}m_H}}\cos\theta\right), \qquad (2)$$

where m_{H^-} and m_H are the masses of H^- and H, respectively, $\mu = m_{H^-}m_H/(m_{H^-} + m_H)$ is the reduced mass of the colliding system, and θ is the angle of intersection. E_r is controlled by leaving U_s constant and varying U_f. This merged-beam approach allows us to reach collision energies on the order of a few meV, limited only by the spread in collision angles between the two beams and the energy spread of each beam [11]. Additionally, due to the high velocity of the collision partners, the angular spread of the reaction products is strongly compressed in the forward direction, allowing their 4π detection on a small surface with standard detector technology.

BPMs are used to determine the beam-beam overlap within the interaction region, which has a length of $L = 96.5 \pm 1.0$ cm. BPM3 is located shortly after the beginning of the interaction region and BPM4 shortly before the end, which is defined by an electrostatic quadrupole deflector used to direct the H^- beam into a Faraday cup (the H^- dump). Any H_2 formed in the interaction region has an energy of essentially $E_{H_2} = E_{H^-} + E_H = -2eU_s = 20$ keV [1].

From the exit of the spherical deflector to the end of the interaction region, compensating magnet coils are mounted in the horizontal and vertical planes parallel to the direction of the beams. These allow us to minimize the deflection of the anion beam by the Earth's magnetic field, thus minimizing the angle between the anion and neutral beams, and thereby maximizing the resolving power of the measurement (i.e., minimizing the energy spread).

After the quadrupole, both the H beam and any AD-generated H_2 continue on into a helium gas cell at $\sim 2 \times 10^{-4}$ Torr. A cleaner electrode immediately before the gas cell removes any H^+ and H_2^+ created upstream of the gas cell. Inside the cell ~5% of the H_2 is ionized by the stripping collision

$$H_2 + He \rightarrow H_2^+ + [He, e^-]. \qquad (3)$$

The final state of the He is unimportant. The resulting ~20 keV H_2^+ is the signal we use to detect reaction (1). In the gas cell, stripping of the H beam and dissociative ionization of the H_2 can each produce ~10 keV H^+.

After the gas cell, the neutrals and resulting ions enter a series of two double-focusing, electrostatic cylindrical deflectors [12]. A hole in the outer plate of the first or lower cylindrical deflector (LCD) allows neutrals to pass through and travel into a neutral particle detector. The neutral particle current is monitored by measuring the secondary negative particle emission from the target inside the neutral detector. The LCD is used to deflect H_2^+ ions upward through a 90° angle. The second or upper cylindrical deflector (UCD) sends the H_2^+ ions through another 90° bend so that they are again flying horizontally, but perpendicular to the original merged-beam axis.

Electrostatic analyzers discriminate charged particles based on their kinetic energy. We set the voltages on the LCD and UCD to transmit the ~20 keV H_2^+ signal ions and direct them into a channel electron multiplier (CEM) while discriminating against any ~10 keV H^+ formed in the gas cell. Any H_2^+ produced in the electric field of the LCD is generated with a velocity vector and at a beam energy that does not lie within the acceptance of the LCD+UCD configuration and is not detected.

Specific apparatus details relevant to the results presented here are discussed in more depth in the subsequent sections of this paper. Additional details of the apparatus can be found in [1] and [10].

B. Rate coefficient measurement

Experimentally, we measure the cross section σ_{AD} for reaction (1) times the relative velocity v_r between the H^- and H beams convolved with the velocity spread of the experiment. This gives the rate coefficient

$$\langle \sigma_{AD} v_r \rangle = R_{H_2}\left(\int_V n_{H^-} n_H dV\right)^{-1}. \qquad (4)$$

Here R_{H_2} is the AD-generated H_2 rate, n_{H^-} and n_H are the respective particle densities of each beam, and the integral is over the volume V of the overlapping beams in the interaction region.

We infer R_{H_2} from the signal $H_2{}^+$ created through the stripping reaction in the He gas cell giving $R_{H_2^+}$. Because we operate at low He target thicknesses (often called the linear regime), we have

$$R_{H_2} = \frac{R_{H_2^+}}{\sigma_{st} N_{He}} \tag{5}$$

where σ_{st} is the single-electron stripping cross section and N_{He} is the helium target column density (or target thickness). The measured stripping cross section for 20 keV H_2 on He is $(1.04 \pm 0.17) \times 10^{-16}$ cm^2 [13]. The $\pm 16\%$ error in σ_{st} represents the largest contribution to the uncertainty of our absolute scale. Here and throughout the paper all uncertainties are given at an estimated 1σ level. An additional 10% uncertainty arises due to the unknown rovibrational distribution of the AD-generated H_2 as we discuss in more detail in [10]. Our determination of N_{He} is presented in detail in Sec. III.

The quantity $R_{H_2^+}$ is given by

$$R_{H_2^+} = \frac{S}{T_a T_g \eta} \tag{6}$$

where S is the background-subtracted $H_2{}^+$ signal rate, the derivation of which is described in Sec. IV. The measured transmittance of the combined LCD and UCD arrangement is $T_a = 0.99 \pm 0.01$; the geometric transmittance of the grid in front of the CEM is $T_g = 0.90$, with an assumed 1% uncertainty; and the CEM detection efficiency is $\eta = 0.98 \pm 0.02$. These three quantities are discussed in more detail in [1].

Focusing now on the term in the parentheses on the right-hand side of Eq. (4), we define the flux for a single beam species i as $J_i = n_i v_i$ where n_i is the particle density of the beam and v_i the beam velocity. This gives

$$\left(\int n_{H^-} n_H dV \right)^{-1} = \left(\frac{1}{v_{H^-} v_H} \int J_{H^-} J_H dV \right)^{-1}. \tag{7}$$

Here v_{H^-} and v_H are the velocities of the H^- and H beams, respectively. Next, for a single species beam i traveling along the z axis, we can make use of the relationship between beam current and beam flux,

$$I_i = \iint q_i J_i(x,y) dx dy, \tag{8}$$

where q_i is the charge per particle. We assume there is no significant current loss as the beam travels along the z axis in the interaction region. So we can now write

$$\int J_{H^-} J_H dV = \frac{I_{H^-}}{q_{H^-}} \frac{I_H}{q_H} \Omega, \tag{9}$$

where I_{H^-} is the H^- current; I_H is the H particle current (expressed here and throughout the paper in amperes); $q_{H^-} = -e$; and with our convention here for I_H, $q_H = -e$. The methods for measuring the ion and neutral currents are discussed in Secs. V and VI, respectively.

The overlap factor Ω is given by

$$\Omega = \frac{\iiint J_{H^-}(x,y,z) J_H(x,y,z) dx dy dz}{\iint J_{H^-}(x,y) dx dy \iint J_H(x,y) dx dy}. \tag{10}$$

In the absence of attenuation, the two-dimensional integrals of J_{H^-} and J_H are conserved (i.e., the particle currents), regardless of z. We define the overlap at any xy plane along the z axis as

$$\Omega(z) = \frac{\iint J_{H^-}(x,y,z) J_H(x,y,z) dx dy}{\iint J_{H^-}(x,y) dx dy \iint J_H(x,y) dx dy} \tag{11}$$

with

$$\Omega = \int \Omega(z) dz. \tag{12}$$

Further simplification is possible by averaging $\Omega(z)$:

$$\langle \Omega(z) \rangle = \frac{1}{L} \int \Omega(z) dz, \tag{13}$$

where the integral is over the interaction length. Determination of $\Omega(z)$ is discussed in detail in Sec. VII.

We can now reexpress $\langle \sigma_{AD} v_r \rangle$ as

$$\langle \sigma_{AD} v_r \rangle = \frac{1}{\sigma_{st} N_{He}} \frac{S}{T_a T_g \eta} \frac{e^2}{I_{H^-} I_H} \frac{v_{H^-} v_H}{L \langle \Omega(z) \rangle}. \tag{14}$$

The average on the left-hand side is over the energy spread of the measurement described in Sec. VII.

III. HELIUM GAS CELL COLUMN DENSITY

The gas cell base pressure with the beams on and no He is $\sim 1 \times 10^{-6}$ Torr. As we operate at typical He pressures of 2×10^{-4} Torr, we can ignore the base pressure contribution to the column density of the gas cell.

The He column density in the gas cell is given by

$$N_{He} = \int_{\text{gas cell}} n_{He}(\ell) d\ell, \tag{15}$$

where $n_{He}(\ell)$ is the He number density along the beam path and $d\ell$ the differential path length. N_{He} can be accurately approximated using the relationship

$$N_{He} = n_{He} L_{st}, \tag{16}$$

where n_{He} is the He density in the gas cell as determined using the pressure gauge reading and L_{st} is the effective stripping length of the gas cell, essentially taking into account any variation in n_{He} along ℓ.

We determine the value of L_{st} using H^- current loss measurements versus gas cell pressure in a separate measurement where we send the H^- beam through the gas cell. For these H^- loss results, the attenuating He column density is given by

$$N'_{He} = \int_{\text{quad}} n_{He}(\ell) d\ell + \int_{\text{gas cell}} n_{He}(\ell) d\ell + \int_{\text{analyzer}} n_{He}(\ell) d\ell. \tag{17}$$

The first integral is over the path length in the quadrupole (quad), the second over the gas cell, and the third in the analyzer. Comparison with Eq. (15) shows that N_{He} is given by the second term on the right-hand side of Eq. (17). As we detect only $H_2{}^+$ generated by stripping in the gas cell,

it is this second term that we need to know in order to put our AD measurements on an absolute scale. But we begin by determining N'_{He} using the H^- current loss method.

The H^- beam is attenuated by single-electron detachment (SED)

$$H^- + He \rightarrow H + [He, e^-] \tag{18}$$

and double-electron detachment (DED)

$$H^- + He \rightarrow H^+ + [He, e^-, e^-] \tag{19}$$

where the final state of the He is unimportant. The total electron detachment (ED) cross section σ_{ED} is given by

$$\sigma_{\mathrm{ED}} = \sigma_{\mathrm{SED}} + \sigma_{\mathrm{DED}}, \tag{20}$$

where $\sigma_{\mathrm{SED}} = (6.14 \pm 0.38) \times 10^{-16}$ cm^2 was measured by [14] and $\sigma_{\mathrm{DED}} = (5.46 \pm 1.64) \times 10^{-17}$ cm^2 is the recommended cross section of [15].

With our experimental configuration SED creates fast H and DED fast H^+. The H can repopulate the parent H^- beam via single-electron capture (SEC) but the recommended value for σ_{SEC} [15] is a factor of ~130 smaller than σ_{SED}. Similarly, the H^+ can repopulate the H^- beam via double-electron capture (DEC), but the recommended σ_{DEC} [15] is a factor of ~540 times smaller than σ_{DED}. Hence we assume that both of these repopulating mechanisms will have an insignificant effect on our results here and can be ignored.

For the H^- attenuation measurements, the initial H^- current is recorded in the H^- dump ($I^{\mathrm{o}}_{\mathrm{H}^-}$). To measure the transmitted current, we use the UCD as a Faraday cup and record $I^{\mathrm{UCD}}_{\mathrm{H}^-}$. We bias the inner plate with a negative voltage to repel any emitted secondary negative particles back onto the outer plate. For no attenuation in the gas cell, excellent agreement was found between the measured currents in the H^- dump and the transmitted currents in either the neutral cup or the UCD deflector.

The attenuated current versus gas density is given by

$$\frac{I^{\mathrm{UCD}}_{\mathrm{H}^-}}{I^{\mathrm{o}}_{\mathrm{H}^-}} = \exp(-\sigma_{\mathrm{ED}} N'_{\mathrm{He}}). \tag{21}$$

Because the pressures in the quad (region 1), the gas cell (region 2), and the analyzer (region 3) all scale linearly with the gas cell pressure [1], we can write

$$N'_{\mathrm{He}} = n_2 L'_{\mathrm{st}}, \tag{22}$$

where we treat the He number density in the gas cell, n_2, as constant along the cell. L'_{st} is the measured effective ED length and incorporates the effects of density gradients as the H^- beam traverses from the quad, through the gas cell, and into the analyzer before it is measured.

From the ideal gas law, one can readily show that the number density of a species and the pressure at room temperature (293 K) are related by

$$n = 3.29 \times 10^{16} p \text{ cm}^{-3}, \tag{23}$$

where p is in Torr. Using this to rewrite Eq. (22) in terms of the gas cell pressure p_2, we find

$$N'_{\mathrm{He}} = 3.29 \times 10^{16} p_2 L'_{\mathrm{st}}. \tag{24}$$

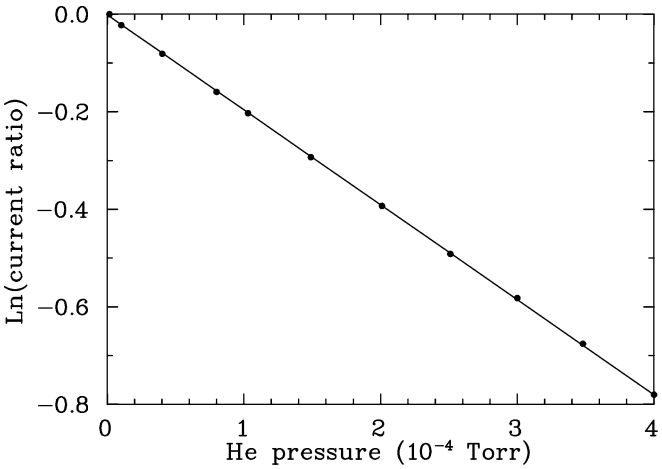

FIG. 2. Ratio of the attenuated H^- current to initial current as a function of the He pressure in the gas cell. The circles are the data and the straight line shows the best fit.

The measured attenuation data for 10 keV H^- versus p_2 are shown in Fig. 2. We have fitted these data using Eqs. (21) and (24). The error of the fit is extremely small (as can be seen from the figure) and makes an insignificant contribution to the uncertainty in the derived value for L'_{st}. Taking into account the published uncertainties in σ_{SED} and σ_{DED} yields $L'_{\mathrm{st}} = 88.4^{+5.8}_{-5.2}$ cm with the error in percentage being +7% and −6%.

At this point we need to create a simple model to convert our measurement of L'_{st} into L_{st}. We do this by making three simplifying approximations for Eq. (17). First, we assume that the pressure gradient at the entrance and exit of the gas cell can be accurately represented as a step function. Second, we treat the gas pressure in each of the three regions as constant along the ion beam. Third, we consider the gas pressure in each section as being accurately given by their respective pressure gauges.

Taking into account the distances from the entrance of the quadrupole to the H^- dump and to the entrance of the gas cell, the H^- dump effectively measures the H^- current at a distance $L_1 = 5.0$ cm before the gas cell entrance. We denote the He pressure and density in this region as p_1 and n_1, respectively. The length of the gas cell is $L_2 = 78.7$ cm. In the final analyzer the H^- travels a distance $L_3 = 35.4$ cm before striking the UCD. The gas pressure is p_3 and the He density n_3.

We can reexpress Eq. (17), giving the attenuating column density that the H^- passes through, as

$$N'_{\mathrm{He}} = n_1 L_1 + n_2 L_2 + n_3 L_3, \tag{25}$$

which we can rewrite as

$$N'_{\mathrm{He}} = n_2 L'_2, \tag{26}$$

where

$$L'_2 = \left(\frac{n_1}{n_2} L_1 + L_2 + \frac{n_3}{n_2} L_3 \right). \tag{27}$$

Attenuation data were collected at He pressures up to $p_2 = 4 \times 10^{-4}$ Torr. Over this range we measured $n_1/n_2 = 0.145$ and $n_3/n_2 = 0.155$, giving $L'_2 = 84.9$ cm. This differs by

-4% from L'_{st}, which we take as an estimate for the uncertainty in our simple model.

Equating $L_{st}/L'_{st} = L_2/L'_2$, we solve for L_{St}, giving the effective gas cell length for stripping of AD-generated H_2,

$$L_{st} = \left(\frac{L_2}{L'_2}\right) L'_{st} = 0.927 L'_{st}. \tag{28}$$

Using the fitted value for L'_{st} and adding the above uncertainties in quadrature gives $L_{st} = 81.9 \pm 5.7$ cm with the error in percentage being $\pm 7\%$. Finally, N_{He} is determined using Eqs. (16) and (23) in combination with the measured value of p_2 and our determination here of L_{st}.

IV. SIGNAL DETERMINATION

Considerable effort was put into suppression of background counts due to particles other than $H_2{}^+$ (including photons). These efforts are reviewed in detail in [1]. As a result, the CEM counts are essentially due only to H_2 molecules formed along the second leg of the apparatus and stripped in the gas cell, with an extremely small dark rate.

The chopping scheme used for data collection is shown in Fig. 3. Four different rates are measured during data acquisition: both beams on (R_1), H^- on and H off (R_2), H^- off and H on (R_3), and both beams off (R_4). Timing details of the chopping pattern are discussed in [1].

We separate the measured rates into those with the laser on ($R_1 - R_3$) and those with the laser off ($R_2 - R_4$). These differences subtract out the dark rate, which is the same for all four portions of the chopping pattern. What remains in the quantity ($R_1 - R_3$) is the $H_2{}^+$ CEM rate arising from H_2 generated in the interaction region due to H^- interacting with H produced both by photodetachment and by stripping. This stripped H can be formed anywhere along the second leg of the apparatus. The quantity ($R_2 - R_4$) is the $H_2{}^+$ CEM rate arising from H_2 generated in the interaction region due to H^- interacting only with H produced by stripping.

To a first approximation, the difference $(R_1 - R_3) - (R_2 - R_4)$ gives the $H_2{}^+$ CEM rate due to H_2 formation solely in the interaction region. What this ignores, however, is that as the laser is chopped, this changes both the H^- beam current and the H created by stripping of the H^- beam. As a result, the H_2 background depends on the laser state.

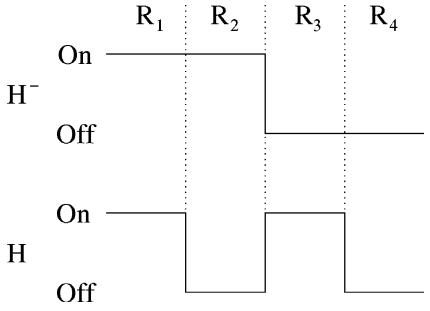

FIG. 3. Schematic of the square wave pattern used for data acquisition. The pattern indicates when the H^- and H beams were on or off in the interaction region. The H^- beam was chopped at 50 Hz and the H beam at 100 Hz. The time duration was equal for each quadrant in the chopping pattern.

In order to determine the true $H_2{}^+$ signal from H_2 generated in the interaction region and subsequently stripped in the gas cell, we need to properly subtract out background H_2 formed by collisions between the H^- beam and H created by stripping of the H^- beam. To this end, it is useful to reexpress Eq. (14) as

$$R_i = \beta I_{H^-} I_H, \tag{29}$$

where R_i is the measured $H_2{}^+$ rate for a particular phase of the chopping cycle ($i = 1$–4) and

$$\beta = \langle \sigma_{AD} v_r \rangle \sigma_{St} N_{He} T_a T_g \eta \frac{L \langle \Omega(z) \rangle}{e^2 v_{H^-} v_H}. \tag{30}$$

The difference in the laser-off rates ($R_2 - R_4$) can now be written as

$$R_2 - R_4 = \beta I^{off}_{H^-} \left(I^u_H + I^d_H\right). \tag{31}$$

Here $I^{off}_{H^-}$ is the cw H^- current in the H^- dump measured with the laser off, I^u_H is the cw atomic H particle current created by stripping of the H^- beam upstream (u) of the photodetachment region, and I^d_H is the cw atomic H particle current created by stripping of the H^- beam downstream (d) of the photodetachment region.

With the laser on, the H^- beam is reduced by a factor

$$f = 1 - I^{on}_{H^-}/I^{off}_{H^-}. \tag{32}$$

For convenience, we rewrite this as

$$I^{on}_{H^-} = (1 - f) I^{off}_{H^-}. \tag{33}$$

The particle current I^u_H is independent of the laser state. However, I^d_H varies with the state of the laser. The majority of I^d_H is formed in the higher-pressure region after the end of the photodetachment chamber (discussed below and also in [1]). The resulting H beam will have nearly the same properties as the parent H^- beam at aperture 2. Hence we expect that I^d_H will be reduced by the same factor of $(1 - f)$ when the laser is on. With the laser on, the photodetached H particle cw current is given by I^{PD}_H. Combining these results, the difference in the laser-on rates $(R_1 - R_3)$ is

$$R_1 - R_3 = \beta (1 - f) I^{off}_{H^-} \left\{ I^{PD}_H + I^u_H + I^d_H (1 - f) \right\}. \tag{34}$$

Defining

$$\delta = \frac{I^d_H}{I^u_H}, \tag{35}$$

we can rewrite Eqs. (31) and (34) as

$$R_2 - R_4 = \beta I^{off}_{H^-} I^u_H (1 + \delta). \tag{36}$$

and

$$R_1 - R_3 = \beta (1 - f) I^{off}_{H^-} \left\{ I^{PD}_H + I^u_H [1 + \delta (1 - f)] \right\}. \tag{37}$$

Solving the first of these equations for I^u_H yields

$$I^u_H = \frac{R_2 - R_4}{\beta I^{off}_{H^-} (1 + \delta)}, \tag{38}$$

which we substitute into the second equation to find

$$R_1 - R_3 = \beta (1 - f) I^{off}_{H^-} I^{PD}_H + (1 - f) \left(\frac{1 + \delta (1 - f)}{1 + \delta} \right) (R_2 - R_4). \tag{39}$$

The true AD signal rate is given by the first term on the right-hand side of Eq. (39):

$$S = \beta(1-f) I_{H^-}^{off} I_H^{PD}, \tag{40}$$

where the $(1-f)$ takes into account that $I_{H^-}^{off}$ is the cw H^- current with the laser off but the signal comes from when the laser is on. Rearranging Eq. (39) and using Eq. (40) we find

$$S = R_1 - R_3 - (1-f)\left(\frac{1+\delta(1-f)}{1+\delta}\right)(R_2 - R_4). \tag{41}$$

We have determined f by measuring $I_{H^-}^{off}$ and $I_{H^-}^{on}$ in the H^- dump under simulated data acquisition conditions. We find $f = 0.074 \pm 0.015$ where the uncertainty is the measured scatter in f at a 1σ level. This error results in only a $\pm 5\%$ uncertainty in S for our results.

The ratio δ is determined by the neutral currents I_H^u and I_H^d which are functions of the column density and the composition of the stripping gas in their respective portions of the second leg of the setup. Differential pumping at the entrance and exit of the photodetachment chamber combined with the influx of helium from the gas cell into the vacuum system upstream of the chopper results in essentially three nearly constant pressure regions: from the spherical deflector exit to the entrance of the photodetachment chamber, the chamber itself, and a short third region from the exit of the chamber to the chopper electrode which is at the same pressure as the interaction region. The pressure in each of these regions is roughly an order of magnitude less than that of the preceding region. As a result of the enhanced pressure and stripping in this third region, more neutrals are created through H^- stripping downstream of the photodetachment region than upstream, giving $\delta > 1$.

Using the measured pressure readings in each section, their respective lengths, VAKLOOP pressure profile simulations [16,17], and the SED cross sections for H^- on He [14] and H_2 [18], we calculate a factor $\delta = 7.2$. Assuming an unrealistically large factor of 2 uncertainty in δ introduces a $\pm 1\%$ error in S for our results here.

Given the above uncertainties for f and δ, we find

$$S = R_1 - R_3 - (0.866 \pm 0.057)(R_2 - R_4), \tag{42}$$

which gives a 5% uncertainty in our results. The uncertainty in S, due to counting statistics in R_1, R_2, R_3, and R_4, is discussed in Sec. X.

There is one background which is subtracted out by beam chopping but which was not explicitly included in Eqs. (31) and (34). As the H^- beam passes through the interaction region (IR), SED off the rest gas creates H which can then react with the parent H^- beam and form H_2. This occurs in both R_1 and R_2 and is almost exactly subtracted out correctly by Eq. (42). We find that adding a term I_H^{IR} to Eqs. (31) and (34) and working through the algebra increases S by only 1%, an insignificant effect which we ignore here.

Lastly, signal H_2 can be destroyed through collisions with the $\sim 3 \times 10^{-5}$ Torr of He in the interaction region. In the linear regime, the fraction destroyed is given by $n_{He}\sigma_{TD}L/2$ where the total destruction (TD) cross section is $\sigma_{TD} \sim 2 \times 10^{-16}$ cm^2 [13,19] and the factor of one-half is to account for the fact that the signal H_2 molecules on average travel only half the length of the interaction region. Using Eq. (23) and plugging in the relevant numbers, we find that less than 1% of the signal H_2 is destroyed before making it into the gas cell. This is an insignificant effect which we ignore here.

V. ANION CURRENT

The H^- current was measured using a picoammeter that averages over the chopping cycle, giving $\langle I_{H^-}^{chop} \rangle$. With the laser off and a 50 Hz chopping frequency, the ratio of the unchopped to the chopped currents was $a = 1.964$. Utilizing an extremely stable fast current amplifier we verified that the deviation from a factor of 2 is due to the internal amplification and averaging mechanisms of the picoammeter.

During data collection, the picoammeter averaged over both the H^- and the laser (i.e., H) chopping patterns. Since the same duration was used for each quadrant of the chopping pattern, we have

$$\langle I_{H^-}^{chop} \rangle = \frac{1}{a}\left(\frac{I_{H^-}^{off}}{2} + \frac{I_{H^-}^{on}}{2}\right). \tag{43}$$

The factors of $1/2$ account for the anions being on for half the time the laser was on and off for the other half.

With the laser on, the H^- beam is reduced by a factor of $1-f$ as discussed in Sec. IV. Using Eqs. (33) and (43), we find for the cw currents $I_{H^-}^{off}$ and $I_{H^-}^{on}$

$$I_{H^-}^{off} = \left(\frac{a}{1-f/2}\right)\langle I_{H^-}^{chop} \rangle \tag{44}$$

and

$$I_{H^-}^{on} = \left(\frac{a(1-f)}{1-f/2}\right)\langle I_{H^-}^{chop} \rangle. \tag{45}$$

A second correction factor is due to attenuation of the H^- beam via ED. The attenuation is insignificant from the beginning of the second leg of the apparatus to the end of the photodetachment chamber, a distance of $\sim$360 cm along which the operating pressure is $\lesssim 5 \times 10^{-7}$ Torr. Modeling indicates that ED becomes important from the exit of the photodetachment chamber to the beginning of the interaction region (29 cm), through the interaction region (96 cm), and extends from there through the quadrupole to the mouth of the H^- dump (8 cm). He flowing out of the differentially pumped gas cell brings the measured operating pressure in this 132-cm-long region to $\sim 3 \times 10^{-5}$ Torr.

We quantified the attenuation by first recording the anion current in the H^- dump with the gas cell at a base pressure of $\sim 1 \times 10^{-6}$ Torr and then at the operating He pressure of 2×10^{-4} Torr. The measured attenuation from the beginning of the interaction region to the H^- dump was 8.6%, indicating we are in the linear regime. This attenuation reduces to 3.6% when averaged over the entire length of the interaction region. Thus the average anion current through the interaction region was a factor of $b = 1/(1-0.036) = 1.04$ times higher than that measured in the H^- dump. Taking this into account gives

$$I_{H^-}^{off} = \left(\frac{ab}{1-f/2}\right)\langle I_{H^-}^{chop} \rangle \tag{46}$$

and

$$I_{H^-}^{on} = \left(\frac{ab(1-f)}{1-f/2}\right)\langle I_{H^-}^{chop} \rangle. \tag{47}$$

The uncertainties in a, b, and f result in an estimated 3% overall error for the anion current measurement.

VI. NEUTRAL CURRENT

Modeling studies indicate that the transmittance of the laser-generated H beam through aperture 2 differs from that for the H^- beam due to space charge effects in the H^- beam. Hence we do not expect that $I_H^{PD} = f I_{H^-}^{off}$. The quantity necessary to analyze our data is the ratio of the laser-produced neutral current to the laser-off anion current with both quantities measured after aperture 2. We denote this neutral-to-anion ratio as

$$f_{nta} = \frac{I_H^{PD}}{I_{H^-}^{off}}. \tag{48}$$

Unfortunately, the neutral detector used for our present results was not designed for absolute measurements of I_H. It was therefore necessary to build and install a properly designed neutral cup, to calibrate it, and then to measure f_{nta} under data collection conditions.

The new neutral detector consists of an electrically isolated 304 stainless target disk with a diameter of 3.18 cm. Mounted in front of this stands a positively biased tube with an inner diameter of 2.54 cm. Both are surrounded by a larger-diameter grounded tube with an annular face plate having an inner diameter of 2.54 cm. This is sufficient to ensure collection of the entire H beam, the diameter of which is ~1.2 cm at the entrance of the neutral detector. We have measured this in two ways. In one instance we removed the neutral detector and installed a Beam Imaging Solutions Model BOS-18 beam observation system based on a microchannel plate and a phosphor screen. In the second, we installed a BPM at the same position.

Fast H atoms that strike the target generate secondary negative particles which are collected on the inner positive tube. This yields the measured neutral detector current I_{ND}. The H current is then given by

$$I_H = \frac{I_{ND}}{\gamma} \tag{49}$$

with γ the secondary negative particle emission factor.

We calibrated γ by measuring the change in H^- current as a function of the change in the He pressure of the gas cell. The transmitted H^- current was measured on the UCD simultaneous with the neutral detector current. Both SED and DED contributed to the attenuation, creating H and H^+, respectively. Conservation of particle current requires that the change in $I_{H^-}^{UCD}$ versus pressure equals the change in I_{H^+} and I_H, giving

$$\Delta I_{H^-}^{UCD} = \Delta I_H + \Delta I_{H^+}. \tag{50}$$

The proton current was not measured but can be estimated for thin column densities from the relationship

$$I_{H^+} = I_H \left(\frac{\sigma_{DED}}{\sigma_{SED}} \right). \tag{51}$$

Using this in combination with Eq. (49), we find for a measured change in the neutral current ΔI_{ND}

$$\gamma = \left(1 + \frac{\sigma_{DED}}{\sigma_{SED}} \right) \frac{\Delta I_{ND}}{\Delta I_{H^-}^{UCD}} = (1.09 \pm 0.03) \frac{\Delta I_{ND}}{\Delta I_{H^-}^{UCD}}. \tag{52}$$

For the last step we have inserted the values for σ_{DED} and σ_{SED} given in Sec. III, introducing a 3% uncertainty. We find typical values for γ of ~2.

Having calibrated our neutral detector, it was possible to measure the neutral-to-anion ratio under data collection conditions. The neutral current under operating conditions is attenuated by stripping and by SEC off the He in the system [18]. Almost all of this attenuation is expected to occur in the gas cell. From the center of the interaction region, through the gas cell, and to the neutral detector, we estimate that these reactions reduce the H current by a factor of 0.91 ± 0.02. Correcting for this and for the attenuation of the H^- beam, we find $f_{nta} = 0.0950 \pm 0.0095$ where the quoted 1σ error represents the scatter in the measured values. This implicitly includes the day-to-day variation in the γ measurement. For the total uncertainty in the neutral current we add in quadrature this scatter and the 3% uncertainty due to σ_{DED} and σ_{SED}, giving a total error of 10%.

Lastly, attenuation of the H beam in the interaction region is expected to be insignificant. The total cross section [18] for this is a factor of ~4.5 times smaller than that for the H^- attenuation in the interaction region. As we are in the linear regime, we expect a similar reduction for the attenuation of the H beam. We therefore estimate that the H beam current is reduced by less than 1%, an insignificant correction which is ignored here.

VII. BEAM OVERLAP AND COLLISION ENERGIES

The overlap of the two beams is determined from a combination of profile measurements and geometric modeling. The overlaps are calculated from the beam profiles recorded by the two BPMs located in the interaction region. We have also performed simulations of the beam trajectories starting at aperture 1 and extending downstream through to the end of the interaction region. Here we describe each method. We also used the geometric modeling to determine the center-of-mass collision energy and energy spread.

A. Overlap determination

Beam profiles are measured in the interaction region using rotating single-wire BPMs to verify that we are working at stable beam conditions and to determine $\Omega(z)$. A detailed discussion of rotating wire BPMs is given in [22]. Only a brief description is presented here.

Each BPM measures a beam profile in two "pseudoplanes" separated by 5.4 cm (±2.7 cm from the center of the BPM). The rotating wire passes the beam horizontally (i.e., along the x axis) in one pseudoplane and vertically (i.e., along the the y axis) in the other pseudoplane. The beam velocity defines the z axis. Given the extremely low divergences of our beams, for a given BPM, we can treat the profiles in the two pseudoplanes as if they were measured at the center of the BPM.

At our beam energies, both charged and neutral beam particles hitting the rotating wire cause secondary negative particles to be emitted. The secondary electrons are then picked up by a shroud lining the inner diameter of the BPM vacuum pipe and connected to a current amplifier. The secondary electron current is proportional to the incident particle current. The measured beam profiles along each axis are in actuality line densities Λ given by the integral expressions

$$\Lambda_i(x) = \epsilon_i \int J_i(x,y)dy, \tag{53}$$

$$\Lambda_i(y) = \epsilon_i \int J_i(x,y)dx, \tag{54}$$

where the index i specifies the beam being scanned. The efficiency factor ϵ_i accounts for the secondary electron emission coefficient of the wire and the efficiency of the electron collection system.

With the laser and chopper off, we record the H^- horizontal and vertical beam profiles at the two BPMs in the interaction region. Then, running the laser in cw mode, and using the chopper electrode to continuously remove the H^- beam before the interaction region, we record the neutral beam profiles at each BPM. For the neutral beam the preamplifier sensitivity of each BPM is electronically increased by a factor of 10.

Representative profiles for both beams in the interaction region are shown in Fig. 4. We also measured the beam profiles by removing the neutral detector and utilizing the BOS-18 beam observation system described in Sec. VI. The recorded profiles were approximately Gaussian in shape. This indicated that the two-dimensional particle densities $J_{H^-}(x,y)$ and $J_H(x,y)$ are separable in x and y. The overlap $\Omega(z)$ at the BPM position z can then be calculated using

$$\Omega(z) = \frac{\int \Lambda_{H^-}(x)\Lambda_H(x)dx \int \Lambda_{H^-}(y)\Lambda_H(y)dy}{\int \Lambda_{H^-}(x)dx \int \Lambda_H(x)dx \int \Lambda_{H^-}(y)dy \int \Lambda_H(y)dy}. \tag{55}$$

Each BPM outputs an analog voltage U proportional to the line density Λ_i of the beam at the corresponding wire position. The output voltage is read into the computer using an analog-to-digital converter at a sampling rate of 3.75 kHz. Any dc offset is subtracted and the profile readings are normalized. We use an arbitrary normalization which ultimately cancels out as each profile appears in both the numerator and denominator of the overlap determination. Due to the sampling at discrete time steps the above integrals become sums over the voltage samples given by

$$\Omega(z) = \frac{\sum_x U_{H^-}(x)U_H(x) \sum_y U_{H^-}(y)U_H(y)}{\sum_x U_{H^-}(x) \sum_x U_H(x) \sum_y U_{H^-}(y) \sum_y U_H(y)}. \tag{56}$$

The BPMs also allowed us to minimize the effects of the Earth's magnetic field on the H^- beam, minimize the angle between the beams, and maximize the overlap of the beams. This was carried out by varying the magnetic field strengths using the compensation coils while monitoring the overlap of the two beams. The resulting full angle between the beam axes in the interaction region was typically ~0.5 mrad (~0.03°). This is far smaller than the maximum 1.79 mrad (0.1°) half angle divergence for each beam set by aperture 1 and 2 and thus makes an insignificant contribution to the energy spread of the measurement.

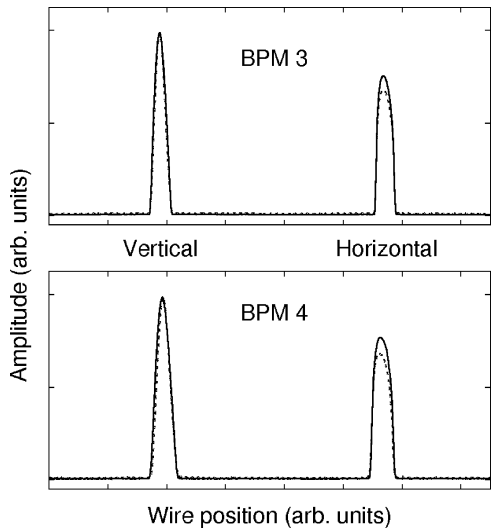

FIG. 4. Vertical and horizontal beam profiles of the H^- beam (solid line) and H beam (dashed line) as a function of the BPM wire position in each beam. The top panel shows the profiles recorded by BPM3 and the bottom panel by BPM4. The left half of each panel shows the vertical beam profiles (y) and the right half the horizontal profiles (x). Both beams have small divergences, resulting in a slightly broader profile in BPM4 compared to BPM3. However, no significant demerging is observed. The widths of the profiles shown are ~5 mm. The overlaps for the profiles shown are 4.21 cm^{-2} for BPM3 and 3.02 cm^{-2} for BPM4.

B. Geometric simulations

1. Overlap determination

Apertures 1 and 2 impose strong geometric limitations on the shape of each beam. As a result we can use ray tracing to model the overlap of the beams, taking the geometric constraints into account. The basic idea behind our ray-tracing model for the propagation of the two beams is shown in Fig. 5. We begin by discretizing into pixels the plane at aperture 1 as well as an xy plane an arbitrary distance d downstream of aperture 2. The simulation then starts at each pixel in aperture 1

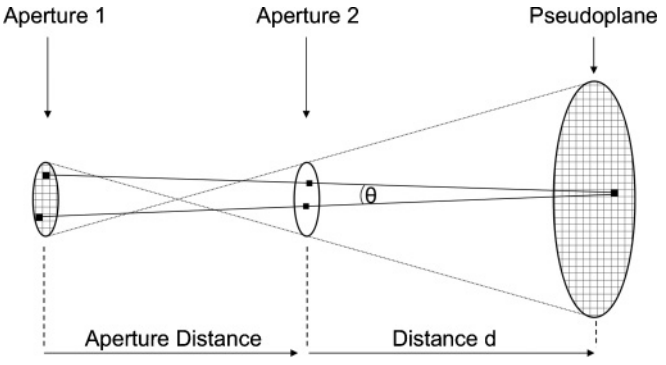

FIG. 5. Schematic overview of the ray-tracing simulation for determining the profile of each beam in the interaction region, the overlap of the two beams, and the relative energy in the center-of-mass frame. See text for additional details.

and calculates all trajectories beginning at aperture 1 that make it through aperture 2 and on to the desired plane. This allows us to calculate the profile of each transmitted beam. Using these results we can then determine how the overlap of the two beams evolves along their respective flight paths by varying d. Comparison of the overlaps from the profile simulation with the measured ones at the two BPM positions showed excellent agreement.

We use these profile simulation results to extrapolate the measured profiles upstream of BPM3, to interpolate between the BPM3 and BPM4 results, and to extrapolate downstream of BPM4. The simulated overlap $\Omega(z)$ is well fitted by a decreasing exponential which we normalize using the BPM3 and BPM4 overlaps and the condition $\Omega(\infty) = 0$. This fit allows us to determine $\langle\Omega(z)\rangle$. Using a less accurate linear function for $\Omega(z)$ results in an $\sim$2% increase in the experimental rate coefficient. The total estimated uncertainty in $\langle\Omega(z)\rangle$ of 3% was derived from a combination of the reproducibility of the BPM overlap measurements and the agreement between two independently written geometric simulations.

2. *Collision energy determination*

We also use the ray-tracing model to determine the mean collision energy $\langle E_r\rangle$ and energy spread versus U_f. We begin at aperture 1 and take all pairs of trajectories emerging from this aperture. Keeping only those pairs that pass through aperture 2 and then cross in the same pixel in the desired xy plane, we calculate the collision angle θ.

For each pair of trajectories, we simulate the energy spread of each beam by assigning each trajectory an energy of $E_{H^-} = -e(U_s + U_f/2) + \delta E_{H^-}$ and $E_H = -e(U_s - U_f/2) + \delta E_H$, respectively. The values for δE_i are randomly chosen from a Gaussian distribution centered around zero with a full width at half maximum of 10 eV. This source energy spread was inferred by chopping the H^- beam and measuring the time-of-flight distribution for the beam. This spread agrees with previously published values for the same type of ion source [23].

From the combined variation in θ and δ_i, we have derived the center-of-mass distribution for E_r at a given floating cell voltage U_f. Figure 6 presents the results in energy. The model probability distribution in velocity is shown in Fig. 7. For floating cell voltages $|U_f| \lesssim 10$ V, E_r is determined largely by the collision angles. The resulting energy spread is reasonably well fit by a Maxwell-Boltzmann (i.e., thermal) distribution. At $|U_f| = 1$ V the distribution corresponds to a temperature of 30 K. As $|U_f|$ increases, the effect of the collision angles becomes less important. For $|U_f| \gtrsim 25$ V the energy spread of the ion source dominates and the distribution becomes Gaussian.

VIII. DATA ACQUISITION PROCEDURE

Each data run typically consisted of 80–100 iterations scanning through a series of floating cell voltages. These scans covered $-1 \geqslant U_f \geqslant -91$ V in steps of 5 V for the lower energies and $-81 \geqslant U_f \geqslant -281$ V in steps of 20 V for the higher energies. Before each run, an intermediate value of U_f was used while the computer automatically tuned the H^- beam. The aim of using an intermediate voltage was to minimize beam changes due to imperfect scaling of the beam optics with U_f.

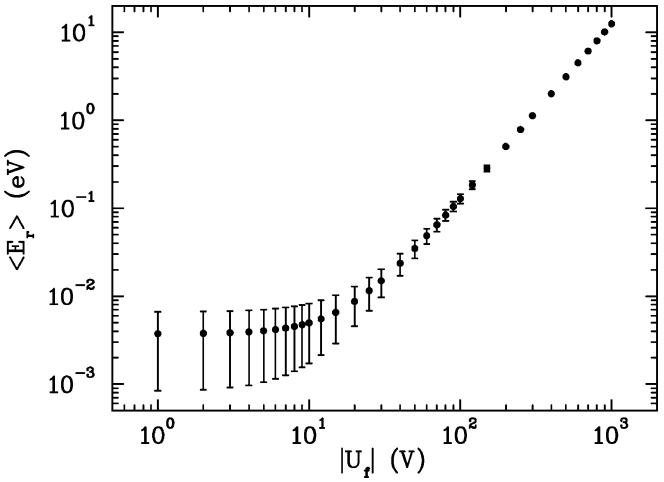

FIG. 6. Calculated average collision energy $\langle E_r\rangle$ (filled circles) and spread (error bars) for different floating cell voltages $|U_f|$ due to collision angles and beam energy spread. Apertures of 5 mm were used for the simulation as were used for the experiment.

A LABVIEW program controlled the data acquisition procedure. After autotuning, beam profiles were recorded for each value of U_f. At each floating cell voltage, first the anion profile was measured and then the neutral beam profile. We also recorded the gas cell pressure reading p_2 whenever beam profiles were taken. For AD data acquisition, all BPMs were turned off with the scanning wire parked at a position outside the beams. Data were then collected for typically 20 iterations after which beam profiles were again recorded. This pattern of autotuning, profile measurements, data collection, and profile measurements was repeated until 80–100 iterations through the selected range for U_f had been performed.

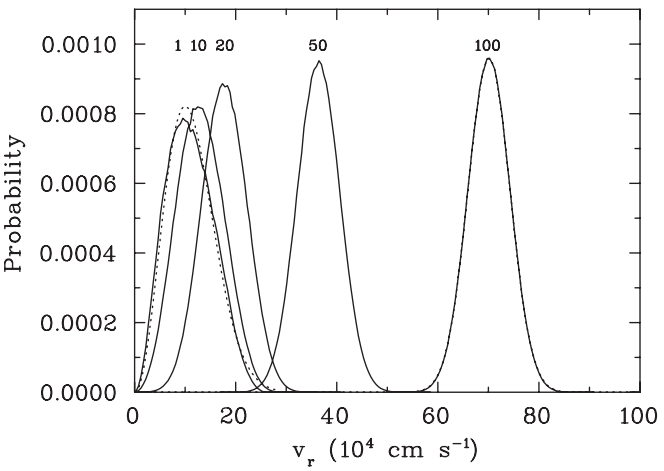

FIG. 7. Collision velocity v_r probability distributions from the geometric simulations described in Sec. VII B. The solid curves from left to right show the results at floating cell voltages of $|U_f| = 1$, 10, 20, 50, and 100 V. The 1 V data have been fitted with a Maxwellian distribution (left dotted curve) and the 100 V data with a Gaussian distribution (right dotted curve) which is not distinguishable from the model results.

TABLE I. Summary of nonstatistical uncertainties going into Eq. (14). Also listed are each relevant symbol, the section where the term is discussed in detail, and typical values. All uncertainties are quoted at a confidence level which is taken to be equivalent to a 1σ statistical confidence level. The uncertainties are also treated as random sign errors and added in quadrature.

Source	Symbol	Section	Value	Error (%)
Stripping cross section	σ_{st}	II	1.04×10^{-16} cm^2	16
Effects of unknown rovibrational distribution	σ_{st}	II		10
Analyzer transmittance	T_a	II	0.99	1
Grid transmittance	T_g	II	0.90	1
CEM detection efficiency	η	II	0.98	2
Overlap length	L	II	96.5 cm	1
He gas cell column density	N_{He}	III	5.4×10^{14} cm^{-2}	7
Signal	S	IV	5 s^{-1}	5
Anion current	I_{H^-}	V	650 nA	3
Neutral current	I_H	VI	62 nA	10
Beam overlap	$\langle\Omega(z)\rangle$	VII	4 cm^{-2}	3
Quadrature sum				24

We acquired AD data using the chopping pattern for each beam shown in Fig. 3. For a given scan, a 5 s dwell time was used for each step in U_f. At the end of each step the rates R_1 through R_4 were recorded as well as the dwell-time-averaged anion current and laser power.

IX. UNCERTAINTIES

The various systematic errors of our measurement are discussed in detail in Secs. II–VII. These systematic uncertainties are quoted at a confidence level believed to be equivalent to a 1σ statistical confidence level. All are summarized in Table I. We treat each as a random sign error and add them all in quadrature. The resulting total estimated systematic uncertainty in our measurement is 24%.

For each data run, the 1σ statistical error at a given E_r is given by simple counting statistics as $\sigma = \pm(R_1 + R_2 + R_3 + R_4)^{1/2}$. Data from all the runs were averaged together at each energy using a $1/\sigma^2$ weighting.

X. RESULTS

A. Experimental rate coefficient

The measured experimental rate coefficient is given by Eq. (14). Sections II–VIII describe the determination of the relevant quantities on the right-hand side of this equation. The resulting AD data are presented as a function of collision energy $\langle E_r\rangle$ in Fig. 8. The circles represent the statistically weighted average of our results and the error bars the 1σ statistical error as described in Sec. IX. Table II lists our results as a function of $|U_f|$ and $\langle E_r\rangle$.

B. Extracted cross section

In order to extract a cross section from our measured $\langle\sigma_{AD} v_r\rangle$, we begin by assuming a functional form for the cross section given by

$$\sigma_{AD}(E_r) = \begin{cases} AE_r^{-B}, & E_r \leqslant E_c, \\ C + DE_r^{-1}, & E_r > E_c. \end{cases} \quad (57)$$

This reproduces the main features of the theoretical cross section from [9]; namely, with increasing energy, a decrease in σ_{AD} more slowly than E_r^{-1} below some critical energy E_c and a decrease as E_r^{-1} for higher energies. Multiplying this by v_r and convolving with the experimental velocity distribution, we obtained the fit parameters A, B, C, D, and E_c via a χ^2 minimization of the difference between the experimental and model results.

Fit parameters are given in Table III and a comparison to theory in Fig. 9. The data point at 4.2 meV was left out of the fit, as it stands out by $\sim$(2–3)σ from the neighboring data points. The fitting incorporated the statistical uncertainties and produced a reduced $\chi^2 = 1.08$. The energy limits of 0.003 eV to 1 eV on the extracted cross section derive from the measured energy range (see Fig. 8 and Table II). We used the covariance matrix of the fit parameters to estimate the standard

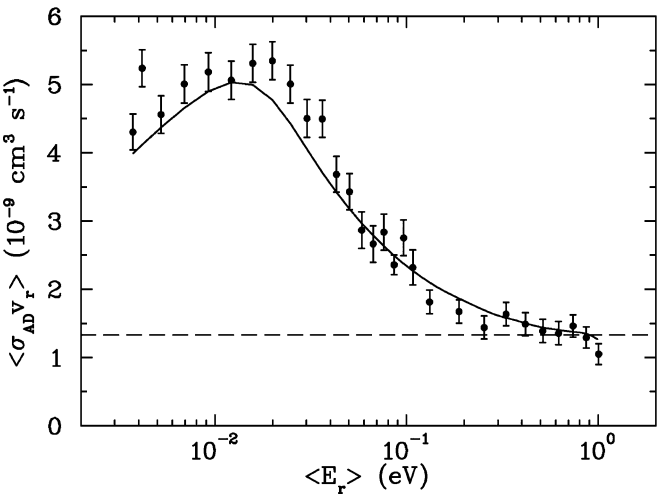

FIG. 8. The experimental rate coefficient $\langle\sigma_{AD} v_r\rangle$ as a function of the collision energy $\langle E_r\rangle$ is shown by the circles and the 1σ statistical uncertainty by the error bars. The solid curve gives the theoretical cross section of [9,10] times the relative velocity convolved with the experimental energy spread. The dashed curve shows the Langevin rate coefficient.

TABLE II. Floating cell voltage $|U_f|$, collision energy $\langle E_r \rangle$, and experimental rate coefficient $\langle \sigma_{AD} v_r \rangle$. The quoted uncertainty represents the 1σ statistical confidence level.

$\lvert U_f \rvert$ (V)	$\langle E_r \rangle$ (eV)	$\langle \sigma_{AD} v_r \rangle$ (10^{-9} cm^3 s^{-1})
1	0.003 74	4.30 ± 0.26
6	0.004 17	5.24 ± 0.27
11	0.005 24	4.56 ± 0.28
16	0.006 93	5.01 ± 0.28
21	0.009 25	5.18 ± 0.28
26	0.0122	5.06 ± 0.28
31	0.0157	5.31 ± 0.28
36	0.0199	5.35 ± 0.28
41	0.0247	5.01 ± 0.28
46	0.0302	4.50 ± 0.28
51	0.0362	4.50 ± 0.27
56	0.0429	3.68 ± 0.26
61	0.0502	3.43 ± 0.26
66	0.0582	2.87 ± 0.27
71	0.0667	2.67 ± 0.27
76	0.0759	2.84 ± 0.26
81	0.0857	2.36 ± 0.14
86	0.0962	2.75 ± 0.26
91	0.107	2.32 ± 0.26
101	0.131	1.81 ± 0.17
121	0.187	1.67 ± 0.17
141	0.252	1.44 ± 0.17
161	0.328	1.64 ± 0.17
181	0.413	1.49 ± 0.17
201	0.509	1.39 ± 0.17
221	0.614	1.36 ± 0.17
241	0.730	1.46 ± 0.16
261	0.855	1.29 ± 0.15
281	0.991	1.05 ± 0.15

deviation of the fit function which we then added quadratically to the systematic experimental uncertainty. The resulting 1σ confidence interval is $\pm 26\%$.

C. Maxwellian rate coefficient

Using our extracted σ_{AD}, we have multiplied this by v_r and convolved it with a Maxwell-Boltzmann thermal velocity distribution. The resulting thermal rate coefficient is shown in Fig. 10 by the solid curve. The results derived from the present experimental work are plotted between 30 and 3000 K. This lower limit corresponds to the energy resolution of the experiment while the upper bound is related to the maximum relative energy covered by the experiment, which was 1 eV.

TABLE III. Fit parameters for Eq. (57) describing the extracted experimental cross section of reaction (1).

Parameter	Value
A (cm^2 eV^{-1})	6.05×10^{-15}
B	0.327
C (cm^2)	2.37×10^{-16}
D (cm^2 eV^{-1})	3.67×10^{-16}
E_c (eV)	0.0158

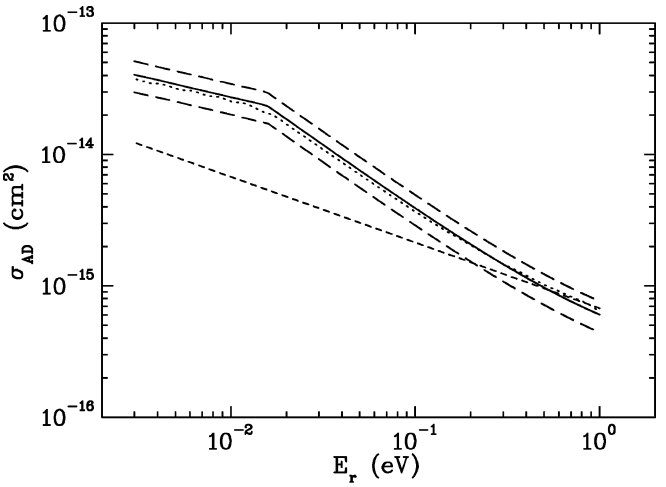

FIG. 9. Extracted experimental cross section for reaction (1) (solid curve) and the total experimental uncertainty at an estimated 1σ level (long-dashed curves). Also shown are the theoretical results from [9,10] (dotted curve) and the Langevin cross section (short-dashed curve).

Indeed, for 3000 K, 11% of the collisions already occur at energies above 1 eV. The error limits shown by the long-dashed curve are those of the extracted cross section.

XI. DISCUSSION

As shown in Fig. 8, we find excellent agreement between our measured $\langle \sigma_{AD} v_r \rangle$ and the calculations of [9,10]. Not surprisingly, this agreement extends to the extracted experimental cross section and the theoretical results of [9,10] as seen in Fig. 9.

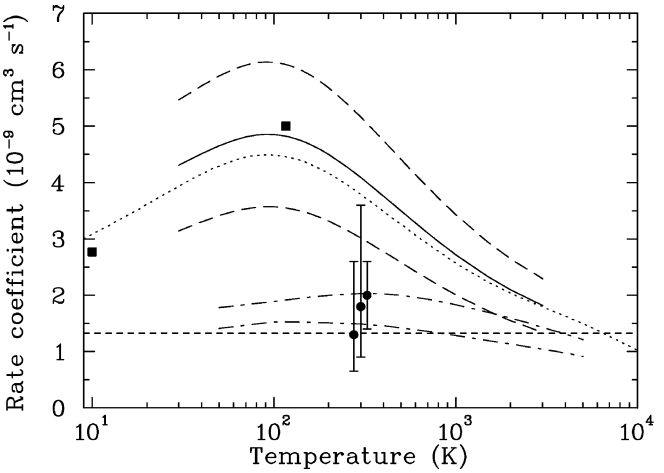

FIG. 10. Thermal rate coefficients for reaction (1) compared to the most recent theoretical results. The solid curve gives the result derived from the present experimental work and the long-dashed curves the estimated 1σ total experimental uncertainty. The circles with the error bars present the 300 K flowing afterglow data of [2], [3], and [4] shifted for clarity by -25 K, 0 K, and +25 K, respectively. Also shown are the theoretical results of [7] for their potential V_1 (upper dotted-long-dashed curve) and V_2 (lower dotted-long-dashed curve), of [8] (squares), and of [9,10] (dotted curve), as well as the Langevin rate coefficient (horizontal short-dashed line).

In Figs. 8 and 9 we also compare our data to the commonly used Langevin theory. Here, though, we have divided the classical Langevin results by a factor of 2 under the assumption that those colliding particles which come in along the H_2^- attractive $X^2\Sigma_u$ potential energy curve (PEC) can undergo AD, but that those which come in along the repulsive $1^2\Sigma_g$ PEC cannot. We find that our experimental results are larger than the Langevin value for collision energies $\lesssim$0.5 eV. We attribute this to the H_2^- PEC being more attractive than the simple polarization case assumed for the Langevin calculations, as has previously been noted by [9].

Concerning thermal rate coefficients, we limit our comparison to only the three most recent theoretical calculations for reaction (1), which are shown in Fig. 10. Our results are discrepant with the theory of [7] over nearly the entire energy range for which the experimentally derived thermal rate coefficient is valid. The reason for this is not known. However, we find good agreement with the calculations of [8] and [9,10].

Previous experimental measurements were performed using flowing afterglows and yielded thermal rate coefficients. Figure 10 presents the afterglow results of [2], [3], and [4]. These first two measurements each have a factor of 2 uncertainty. This reduces their utility. So we limit our discussion to the more recent 300 K results from [4] of $(2.0 \pm 0.6) \times 10^{-9}$ cm^{3}s^{-1}, which are discrepant with our results. A possible explanation for this discrepancy could be that in [4] the neutral H density was determined by normalizing to a measurement by [24] for the AD reaction

$$H + Cl^- \rightarrow HCl + e^-. \quad (58)$$

However, the measurement of [24] is a factor of $\sim$1.5 times smaller than the calculations of [25]. Scaling the data of [4] up by this factor brings them into agreement with our experimental results and with the calculations of [9,10].

The possibility that the results of [24] may be low by a factor of 1.5 is potentially an issue of major concern for astrochemistry. An array of molecular anions have been recently been discovered in interstellar and circumstellar environments [26–30]. These anions can undergo AD with cosmically abundant H, affecting both the molecular abundances and the ionization balance of these astrophysical environments. As a result, researchers have begun measuring AD rate coefficients of various molecular anions with H using flowing afterglows (e.g., [31,32]). However, these researchers have normalized their results to those of [24] to determine the neutral H density. In order to reliably set the absolute value of these normalized AD results, it is clear that a re-measurement of reaction (58) is called for, using a technique other than the flowing afterglow method.

XII. SUMMARY

We have performed absolute measurements for the fundamental anion-neutral reaction $H + H^- \rightarrow H_2 + e^-$. Our results are obtained as a function of energy and are in excellent agreement with the calculations of [8] and [9,10] but discrepant with those of [7]. Our results are also discrepant with the recent room temperature, flowing afterglow measurements of [4]. Future experimental plans include extending our measurements to energies $\langle E_r \rangle$ above 1 eV and investigating the isotope effect by measuring $D + D^- \rightarrow D_2 + e^-$.

ACKNOWLEDGMENTS

The authors thank V. M. Bierbaum and M. Čížek for stimulating discussions, M. Lestinsky, S. A. Marino, B. Reichborn-Kjennerud, and B. L. Schmitt for technical assistance, and D. Thomas for his skilled machining work. This work was supported in part by NSF Grants No. CHE-0520660, No. AST-0606960, and No. AST-0807436. H.B. was supported in part by the German academic exchange service DAAD.

[1] H. Bruhns *et al.*, Rev. Sci. Instrum. **81**, 013112 (2010).
[2] A. L. Schmeltekopf, F. C. Fehsenfeld, and E. E. Ferguson, Astrophys. J. **148**, L155 (1967).
[3] F. C. Fehsenfeld, Carleton J. Howard, and E. E. Ferguson, J. Chem. Phys. **58**, 5841 (1973).
[4] O. Martinez Jr., Z. Yang, N. B. Bettes, T. P. Snow, and V. M. Bierbaum, Astrophys. J. **705**, L172 (2009).
[5] J. C. Browne and A. Dalgarno, J. Phys. B **2**, 885 (1969).
[6] R. J. Bieniek and A. Dalgarno, Astrophys. J. **228**, 635 (1979).
[7] J. M. Launay, M. Le Dourneuf, and C. J. Zeippen, Astron. Astrophys. **252**, 842 (1991).
[8] K. Sakimoto, Chem. Phys. Lett. **164**, 294 (1989).
[9] M. Čížek, J. Horáček, and W. Domcke, J. Phys. B **31**, 2571 (1998).
[10] H. Kreckel, H. Bruhns, M. Čížek, S. C. O. Glover, K. A. Miller, X. Urbain, and D. W. Savin, Science **329**, 69 (2010).
[11] R. A. Phaneuf, C. C. Havener, G. H. Dunn, and A. Müller, Rep. Prog. Phys. **62**, 1143 (1999).
[12] H. Kreckel, H. Bruhns, K. A. Miller, E. Wåhlin, A. Davis, S. Höckh, and D. W. Savin, Rev. Sci. Instrum. **81**, 063304 (2010).
[13] R. Browning, C. J. Latimer, and H. B. Gilbody, J. Phys. B **3**, 667 (1970).
[14] T. J. Kvale, J. S. Allen, X. D. Fang, A. Sen, and R. Matulioniene, Phys. Rev. A **51**, 1351 (1995).
[15] Atomic Data for Fusion. Volume 1: Collisions of H, H_2, He, and Li Atoms and Ions with Atoms and Molecules, Controlled Fusion and Atomic Data Center, edited by C. F. Barnett, Oak Ridge National Laboratory Report No. ORNL-6086, 1990 (unpublished).
[16] V. Ziemann, Vacuum Tracking, SLAC Technical Report No. SLAC-Pub-5962, 1992 (unpublished).
[17] V. Ziemann, Vacuum **81**, 866 (2007).
[18] H. Tawara, At. Data Nucl. Data Tables **22**, 491 (1978).
[19] J. Tabet, S. Eden, F. Gobet, B. Farizon, M. Farizon, S. Ouaskit, P. Scheirer, and T. D. Märk, Int. J. Mass. Spectrom **272**, 48 (2008).
[20] S. J. Smith and D. S. Burch, Phys. Rev. Lett. **2**, 165 (1959).
[21] H.-P. Popp and S. Kruse, J. Quant. Spectrosc. Radiat. Transfer **16**, 683 (1976).

[22] D. G. Seely, H. Bruhns, D. W. Savin, T. J. Kvale, E. Galutschek, H. Aliabadi, and C. C. Havener, Nucl. Instrum. Methods Phys. Res. A **585**, 69 (2008).
[23] C. C. Havener, M. S. Huq, H. F. Krause, P. A. Schulz, and R. A. Phaneuf, Phys. Rev. A **39**, 1725 (1989).
[24] C. J. Howard, F. C. Fehsenfeld, and M. McFarland, J. Chem. Phys. **60**, 5086 (1974).
[25] K. Houfek, M. Čížek, and J. Horáček, Phys. Rev. A **66**, 062702 (2002).
[26] M. C. McCarthy, C. A. Gottlieb, H. Gupta, and P. Thaddeus, Astrophys. J. Lett. **652**, L141 (2006).
[27] J. Cernicharo, M. Guelin, M. Agundez, K. Kawaguchi, M. McCarthy, and P. Thaddeus, Astron. Astrophys. **467**, L37 (2007).
[28] S. Brünken, H. Gupta, C. A. Gottlieb, M. C. McCarthy, and P. Thaddeus, Astrophys. J. Lett. **664**, L43 (2007).
[29] P. Thaddeus, C. A. Gottlieb, H. Gupta, S. Brünken, M. C. McCarthy, M. Agundez, M. Guelin, and J. Cernicharo, Astrophys. J. **677**, 1132 (2008).
[30] J. Cernicharo, M. Guelin, M. Agundez, M. C. McCarthy, and P. Thaddeus, Astrophys. J. Lett. **688**, L83 (2008).
[31] B. Eichelberger, T. P. Snow, C. Barckholtz, and V. M. Bierbaum, Astrophys. J. **667**, 1283 (2007).
[32] T. P. Snow, M. Stepanovic, N. B. Betts, B. R. Eichelberger, O. Martinez Jr., and V. M. Bierbaum, Astrobiology **9**, 1001 (2009).